






Probing the mesoscopic size limit of quantum anomalous Hall insulators

Peng Deng¹, Christopher Eckberg^{2,3,4}, Peng Zhang¹, Gang Qiu¹, Eve Emmanouilidou⁵, Gen Yin¹, Su Kong Chong¹, Lixuan Tai¹, Ni Ni⁵ & Kang L. Wang^{1,5}

The inelastic scattering length (L_s) is a length scale of fundamental importance in condensed matters due to the relationship between inelastic scattering and quantum dephasing. In quantum anomalous Hall (QAH) materials, the mesoscopic length scale L_s plays an instrumental role in determining transport properties. Here we examine L_s in three regimes of the QAH system with distinct transport behaviors: the QAH, quantum critical, and insulating regimes. Although the resistance changes by five orders of magnitude when tuning between these distinct electronic phases, scaling analyses indicate a universal L_s among all regimes. Finally, mesoscopic scaled devices with sizes on the order of L_s were fabricated, enabling the direct detection of the value of L_s in QAH samples. Our results unveil the fundamental length scale that governs the transport behavior of QAH materials.

¹Department of Electrical and Computer Engineering, University of California Los Angeles, Los Angeles, CA, USA. ²Fibertek Inc, Herndon, VA, USA. ³US Army Research Laboratory, Adelphi, MD, USA. ⁴US Army Research Laboratory, Playa Vista, CA, USA. ⁵Department of Physics and Astronomy, University of California Los Angeles, Los Angeles, CA, USA. ✉email: dengpeng@ucla.edu; chris.eckberg@fibertek.com; wang@ee.ucla.edu

The inelastic scattering length, L_s , is the characteristic distance that an electron travels between dephasing inelastic scattering events. It is a length scale below which quantum phase coherence is maintained at non-zero temperatures, playing a pivotal role in certain transport phenomena in condensed matters^{1–8}. Above this length scale, the electrons diffuse classically, without any quantum interference effects. In this sense, while a sample can possess physical dimensions of arbitrary size, L_s sets a fundamental bound for the mesoscopic coherent transport, beyond which transport quantities, e.g. the conductance, scale with the size of the sample^{2,3}. Usually, L_s is temperature-dependent and has the form of $L_s(T) = aT^{-p/2}$, where p is the temperature exponent^{3,9,10}. The value of p depends on material details, such as the scattering mechanism and dimensionality of the system⁴.

As a key determiner of quantum transport phenomena, L_s is known to play a critical role in the quantum critical regime of quantum Hall (QH) and quantum anomalous Hall (QAH) materials. In these prototypical quantum systems, metal-insulator transitions occur when the system is tuned between adjacent Hall plateaus by the magnetic field. During the transit, the physical properties of the system have been demonstrated to depend uniquely upon the ratio between L_s and the diverging critical fluctuation correlation length ξ , as described by finite-size scaling phenomenology^{11,12}. While L_s , and particularly its power-law dependencies, have been well characterized in the critical regime for the QH systems^{13,14}, a comprehensive study of L_s in the quantum critical regime of QAH materials is still lacking. Moreover, the systematic effort undertaken to probe L_s deep within the metallic¹⁵ and insulating phases of QAH samples has been very limited to date. Given the potentially powerful technological implications of the dissipationless transport observed in the former, and the anomalously low temperatures required for this behavior to manifest, the systematic characterization of L_s in the quantized regime in particular could expand the fundamental understanding of the QAH phase in such a way as to potentially guide future material improvements.

Results

QAH, quantum critical, and insulating regimes of the QAH insulator. The QAH effect was theoretically predicted and experimentally realized in Cr- and V- doped topological insulators^{16–20}, and recently has also been observed in MnBi_2Te_4 ²¹ and moiré heterostructures^{22,23}. By manipulating the material's magnetization, QAH systems can be tuned into different phases, namely the QAH, quantum critical, and insulating regimes. Figure 1a, b present the field dependences of Hall conductance (σ_{yx}) and longitudinal resistance (ρ_{xx}), respectively, of a 6-quintuple-layer thick Cr-doped $(\text{BiSb})_2\text{Te}_3$ sample, in which three distinct regimes can be seen. In the QAH regime where the system is fully magnetized, $|\sigma_{yx}|$ exhibits a quantized value of e^2/h . In this phase, the system is highly conductive; displaying a ρ_{xx} of only a few Ohms. That ρ_{xx} is almost vanishing indicates electrons travel with negligible dissipation in the sample. At the opposite extreme near the coercive field (H_c) where equally populated up and down magnetic domains coexist, the system becomes highly resistive as ρ_{xx} reaches a large value (>450 kΩ). Meanwhile, σ_{yx} develops two plateaus with zero conductance, a hallmark of the insulating state²⁴. The QAH and the insulating regime are bridged by the quantum critical regime, wherein σ_{yx} transitions between adjacent plateaus, as will be discussed later. During the phase transition, the conductivities follow a semicircle relation^{25–28}: $\sigma_{xx}^2 + (\sigma_{xy} - \frac{e^2}{2h})^2 = (\frac{e^2}{2h})^2$, as shown in Fig. 1c. At the quantum critical point, $\sigma_{xx} \sim \sigma_{yx} \sim 0.5 e^2/h$.

The three regimes show distinct transport behavior in the temperature dependence of ρ_{xx} , as shown in Fig. 1d. In the figure, each curve was plotted under a constant B^* , where $B^* = B - \mu_0 H_c$ and B is the external magnetic field. Here, using B^* instead of B ensures each temperature-dependent curve was taken under a fixed magnetization rather than a fixed magnetic field. As the sample's internal magnetization is the tuning parameter that drives the QAH phase transition²⁴, such a transformation assists in tracking the QAH transition over wide temperature ranges wherein the magnetic properties are also evolving. In the $T \rightarrow 0$ limit, ρ_{xx} approaches zero and displays a “metallic” behavior in the QAH regime (large B^*), while in the insulating regime ($B^* = 0$), ρ_{xx} diverges and displays an “insulating” behavior. At an intermediate field ($B_c^* = 0.045$ T) corresponding to the quantum critical regime, ρ_{xx} is almost temperature-independent with a critical resistance of $\sim h/e^2$, a value commonly seen in the 2D metal-insulator transition^{29,30}.

The temperature exponent in different regimes. The inelastic scattering length and the temperature exponent p in the QAH, quantum critical, and insulating regimes, respectively, can be obtained by examining the current heating effect³. At low temperatures, the coupling between the electrons and phonons is very weak. In this regime, the electrons can gain additional kinetic energy when subjected to a large electric field, driving them out of thermal equilibrium with the lattice. This kinetic energy gain can be modeled as an increase in the effective temperature of the electronic system through the relationship $k_B T_e \sim eEL_s$, where eEL_s is the average kinetic energy accumulated by electrons between relaxation events and $k_B T_e$ is the effective thermal energy it corresponds to. Since L_s depends on temperature, $L_s \sim T_e^{-p/2}$, the effective temperature would have a power-law relationship with the applied field (or the voltage) as $T_e \sim E^{2/(2+p)}$ ($\sim V^{2/(2+p)}$). The value of p can thus be obtained by carefully monitoring the electric field dependence of T_e . In the quantum critical, QAH, and insulating regimes, this is accomplished by measuring the maximum slope of the Hall conductance $(\partial\sigma_{xy}/\partial B)_{\max}$, the residual resistance of ρ_{xx} and the longitudinal resistance peak (ρ_{xx}^{peak}), respectively, as discussed below.

In the quantum critical regime, the QAH system experiences a metal-insulator transition as σ_{xy} transitions between adjacent plateaus^{26,28,31,32}. According to the finite-size scaling ansatz^{11,12,33,34}, the maximum slope of σ_{xy} , $(\partial\sigma_{xy}/\partial B)_{\max}$ during the transition, exhibits a power-law scaling relationship with the temperature as $(\partial\sigma_{xy}/\partial B)_{\max} \sim T^{-\kappa}$, where κ is the temperature scaling critical exponent. When held at a fixed temperature, $(\partial\sigma_{xy}/\partial B)_{\max}$ also displays a scaling relationship with the current as $(\partial\sigma_{xy}/\partial B)_{\max} \sim I^{-b}$, where b is the current scaling critical exponent^{9,11,12}. These exponents κ and b are themselves convolutions of correlation length exponent ν and temperature exponent p , satisfying the relationships^{35,36}: $\kappa = p/2\nu$ and $b = p/(p+2)\nu$, thus the value of p can be obtained via experimentally measured values of κ and b .

Figure 2a presents the field dependence of σ_{xy} for varying temperatures, showing that the transitions between σ_{xy} plateaus broaden as the temperature increases. Plotted in a log-log plot (Fig. 2b), $(\partial\sigma_{xy}/\partial B)_{\max}$ displays a linear relationship with T , indicating the predicted scaling relationship $(\partial\sigma_{xy}/\partial B)_{\max} \sim T^{-\kappa}$. From the linear fit of the slope, we extracted the exponent $\kappa = 0.63 \pm 0.01$. Meanwhile, Fig. 2c presents the field dependence of σ_{xy} for different currents. Fitting these data we find $(\partial\sigma_{xy}/\partial B)_{\max} \sim I^{-b}$, wherein $b = 0.31 \pm 0.01$ (Fig. 2d). Note that $(\partial\sigma_{xy}/\partial B)_{\max}$ saturates at small currents. In this saturated regime,

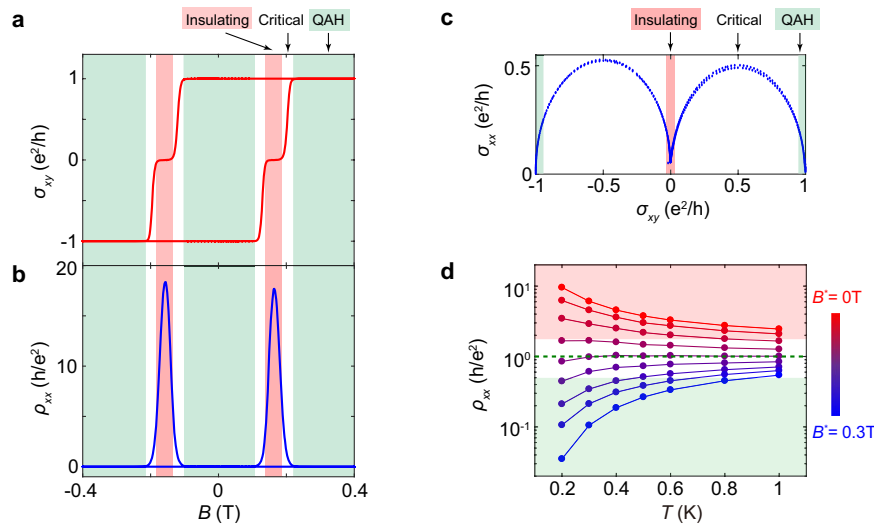


Fig. 1 QAH, quantum critical, and insulating regimes of QAH. **a, b** Magnetic field dependence of σ_{xy} and ρ_{xx} measured at 50 mK. Upon field sweeping, the QAH system can be tuned into the QAH, quantum critical, or insulating regime. **c** Plot of σ_{xx} as a function of σ_{xy} . A semicircle relationship is shown during the transition. **d** Temperature dependence of ρ_{xx} under different B^* , where $B^* = B - \mu_0 H_c$ and H_c is the coercive field, exhibiting a magnetization driven metal-insulator transition at $B^* = B_c^*$ (dashed green line) with a critical resistance of $-h/e^2$.

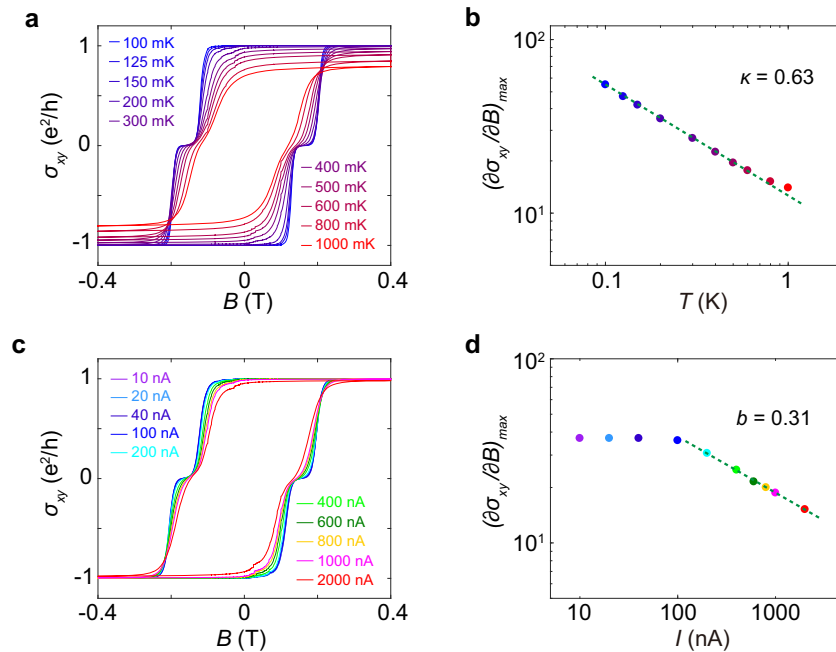


Fig. 2 Scaling behaviors and critical exponents in the quantum critical regime. **a** Field dependence of σ_{xy} at different temperatures. All curves are measured using a 10 nA excitation current. **b** Temperature dependence of $(\partial\sigma_{xy}/\partial B)_{\max}$, demonstrating a temperature scaling relationship as $(\partial\sigma_{xy}/\partial B)_{\max} \sim T^{-\kappa}$. **c** Field dependence of σ_{xy} at different currents. All curves are measured at 200 mK. **d** Current dependence of $(\partial\sigma_{xy}/\partial B)_{\max}$, demonstrating a current scaling relationship as $(\partial\sigma_{xy}/\partial B)_{\max} \sim I^{-b}$ under large currents. The saturation of $(\partial\sigma_{xy}/\partial B)_{\max}$ at $I = 100$ nA indicates the effective temperature is comparable to the bath temperature at this current. From the scaling relationship $(\partial\sigma_{xy}/\partial B)_{\max} \sim T^{-\kappa} \sim I^{-b}$, we have $p = 2.06$.

the effective temperature due to the current heating is lower than the bath temperature. Combining the temperature and current scaling results, we find $p = 2.06 \pm 0.14$.

In the QAH regime where the system is fully magnetized, the longitudinal resistance is exceptionally small and the Hall resistance is quantized. Therefore, a current sourced along the longitudinal direction will produce an electric field predominantly along the transverse direction $E \approx E_y \sim V_{yx}/W = Ih/e^2W$, where E_y and V_{yx} are the Hall electric field and Hall voltage, respectively, I is the applied current, and W is the width of the Hall-bar device.

Figure 3a presents the current dependence of ρ_{xx} under different temperatures (the same plot for ρ_{yx} is shown in Supplementary Fig. 2). For all temperatures, ρ_{xx} maintains a constant value for relatively small currents. Once the current exceeds a temperature-dependent critical value, however, ρ_{xx} begins to increase, indicating that the electrons are heated above the bath temperature by the large electric field. We also measure the temperature dependence of ρ_{xx} as shown in Supplementary Fig. 3, where a small current of 10 nA is applied in order to minimize the current heating effect. By mapping the I (or V_{yx})-dependent ρ_{xx} curve to the T -dependent ρ_{xx}

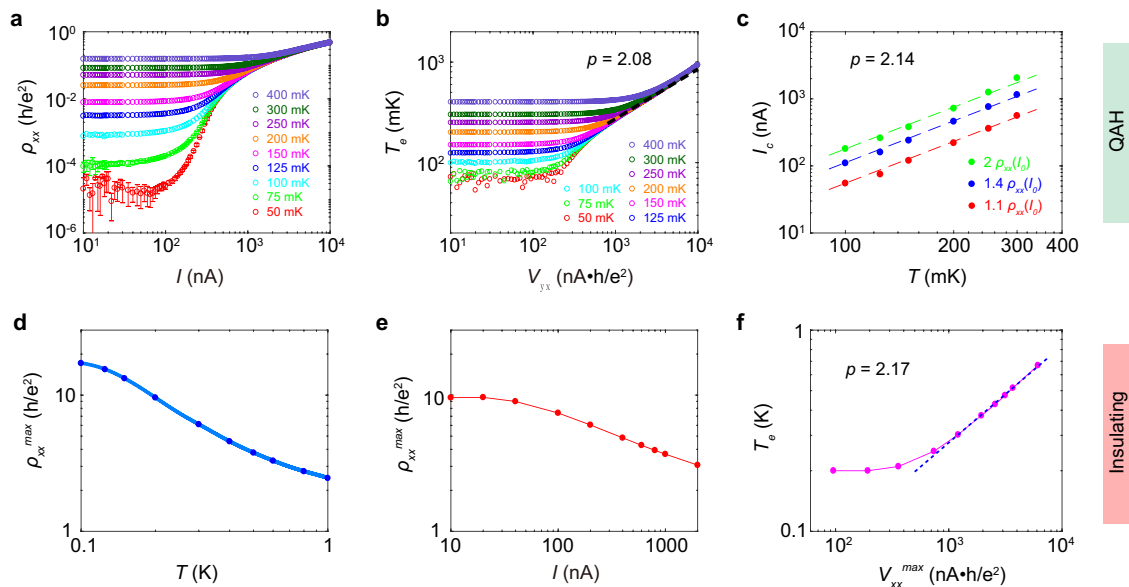


Fig. 3 Critical exponent in the QAH and insulating regimes. **a** Current dependence of ρ_{xx} at various temperatures. All data are measured under a 1 T magnetic field. **b** Effective temperature T_e vs. Hall voltage V_{yx} . Under small currents, T_e equals the bath temperature. As the current increases, the electrons are dominantly thermalized by the electric field, and all data approach a universal curve (fitted by the black dashed lines) with a slope of $2/(p+2) = 0.49$, yielding $p = 2.08$ in the QAH regime. **c** Temperature dependence of I_c . The breakdown current at a given temperature is defined as the current at which ρ_{xx} exceeds m times of ρ_{xx} measured at the base current, where $m = 1.1$ (red), 1.4 (blue), or 2 (green). The slope of the I_c vs. T curve in the log-log plot gives $p = 2.14$. **d** Temperature dependence of ρ_{xx}^{max} . The blue dots are obtained from the resistance maximum in the field-dependent ρ_{xx} curves measured at different temperatures and the cyan lines are extrapolated from the blue dots. **e** Current dependence of ρ_{xx}^{max} . **f** Effective temperature T_e vs. voltage V_{xx}^{max} , under large currents the slope in the log-log plot is $2/(p+2) = 0.48$, yielding $p = 2.17$ in the insulating regime.

curve, the effective temperature plot as a function of V_{yx} can be obtained as shown in Fig. 3b. The linear relationship in the log-log plot at high currents indicates the power-law relationship between T_e and V_{yx} : $T_e \sim V_{yx}^{2/(2+p)}$. From the linear fit of the slope, the value of the temperature exponent p is determined to be $p = 2.08 \pm 0.03$.

The temperature exponent in the QAH regime can also be obtained from the breakdown current (I_c). For each temperature, we define the current at which ρ_{xx} exceeds $m \times \rho_{xx}(I_0)$ as the breakdown current $I_c(T)$, where $I_0 = 10$ nA and m is varied to demonstrate that the physics presented is independent of the precise definition of the breakdown condition. That ρ_{xx} starts to deviate from $\rho_{xx}(I_0)$ at I_c indicates the effective temperature is comparable to the bath temperature under this current. Figure 3c presents the temperature dependence of I_c for $m = 1.1, 1.4,$ and 2 . As can be seen, I_c displays a linear relationship with T in the log-log plot. Since $I_c \sim V_{yx} \sim T^{(p+2)/2}$, we have $p = 2.14 \pm 0.02$ for all m . Notably, the p value obtained from breakdown currents is close to that obtained from high current results discussed above. Previous studies attribute the mechanism of the current breakdown in QAH samples to the field-assisted variable range hopping or bootstrap electron heating^{15,37}. Here the results show that the breakdown of QAH under large current shares the same origin as the breakdown against thermal excitation. Therefore, we anticipate that achieving QAH with a higher quantization temperature would also improve the maximum current they can sustain, which is of great practical use in the application of dissipationless transport.

Finally, in the insulating regime where the QAH sample is at its coercive field, the topological edge transport is suppressed. However, percolative longitudinal transport still occurs²⁴, displaying an insulating temperature dependence. By tracking the temperature and current dependencies of this maximal resistance, the critical exponent p can be extracted in this insulating phase.

At the coercive field, since ρ_{xx} is large and ρ_{yx} becomes zero, the electric field lies predominantly along the longitudinal direction, *i.e.*, $E \approx E_x \sim V_{xx} = I \rho_{xx}^{max}$, where V_{xx} is the voltage drop along the longitudinal direction. The temperature dependence of ρ_{xx}^{max} is obtained by extracting the maximum value in the field-dependent ρ_{xx} isotherms measured with small excitation currents (Supplementary Fig. 4a). As can be seen in Fig. 3d, ρ_{xx}^{max} displays a monotonic decrease with increasing temperature. Likewise, from the field dependence of ρ_{xx} measured under different currents (Supplementary Fig. 4b), the current dependence of ρ_{xx}^{max} can be obtained, as shown in Fig. 3e. By comparing the data points in the ρ_{xx}^{max} vs. I curve and the ρ_{xx}^{max} vs. T curve, each voltage drop at ρ_{xx}^{max} , V_{xx}^{max} , can be one-to-one mapped to an effective temperature T_e , as shown in Fig. 3f. Under high voltages, T_e displays a linear relationship with V_{xx}^{max} in the log-log plot, the slope of which gives a temperature exponent value of $p = 2.17 \pm 0.02$ in this insulating regime.

Despite the dramatic change in conduction behaviors across the different field-driven phases of the QAH material, the value of p shows strikingly little variation; with observed values of 2.06, 2.14, and 2.17 in the critical, QAH, and insulating regimes respectively. As the value of p describes the reduction of the inelastic scattering length with temperature, and generally reflects the dominant excitations from which electrons scatter, this observation indicates the electrons interact with their environment identically in all transport regimes. Such a result indicates a universal transport behavior in the QAH system, and supports theoretical suggestions that a single Hamiltonian can describe the QAH system throughout the plateau-plateau transition³⁸. We would like to note, however, that different values for p are commonly reported in different QH systems, where variations are commonly attributed to differences in the quenched disorders hosted by the materials^{13,39,40}. As such, we do not expect this value of p to necessarily be universal across different QAH samples. On the other hand, a universal value of p is revealed

within individual QAH samples, due to the fact that the quenched disorder remains fixed when samples are tuned across different conduction regimes. We further note that the value of p observed here is close to the value of $p = 2$ that is commonly reported for QHE materials dominated by electron–electron scattering, suggesting a similar mechanism may dominate these QAH samples^{14,35,41–46}.

Estimation of the inelastic scattering length in different regimes. In an effort to further characterize inelastic scattering in the QAH system, we now analyze the absolute value of L_s in the critical, QAH, and insulating regimes. As p is determined for these regimes, obtaining L_s at any given temperature, e.g., 200 mK, would disclose L_s at all temperatures via the relationship $L_s(T) = aT^{-p/2}$. The effective temperature resulting from the current heating effect can be expressed as³ $\pi k_B T_e = 4eEL_s$. Therefore, the inelastic scattering length can be estimated if the electric field at this temperature is known for three regimes, as illustrated below.

1. In the quantum critical regime, both ρ_{xx} and ρ_{yx} exhibit values close to the resistance quantum $\sim h/e^2$, therefore the electric field has components along both longitudinal and transverse directions with $E_y = I\rho_{yx}/W$ and $E_x = I\rho_{xx}/W$, wherein the width of the Hall-bar $W = 0.5$ mm. As shown in Fig. 2d, the increasing trend of $(\partial\sigma_{xy}/\partial B)_{\max}$ with decreasing current saturates at 100 nA, indicating the effective temperature is comparable to the bath temperature 200 mK at this current, giving $L_s \sim 1.85$ μm in this regime.
2. In the QAH regime, $E \approx E_y = I\rho_{yx}/W$. As discussed above, the effective temperature is comparable to the bath temperature when $I = I_c$. It can be seen in Fig. 3c, at 200 mK, $I_c = 220$ nA (for $m = 1.1$), therefore, L_s is estimated to be ~ 1.19 μm in the QAH regime.
3. In the insulating regime at the coercive field, ρ_{xx} is large and ρ_{yx} is around zero. Therefore, $E \approx E_x = V_{xx}^{\max}/L$ and L is the effective length of the Hall-bar devices. As evidenced in Fig. 3f, the effective temperature is about 200 mK when $V_{xx}^{\max} = 192.5$ nA·h/e². Thus, the estimated L_s is ~ 1.36 μm in the insulating regime.

The above results show that the value of L_s in these three distinct regimes not only share a universal temperature exponent p but also have the same order of magnitude at 200 mK, despite the 5 orders of magnitude change in resistance and the transition from “metallic” to “insulating” temperature dependences between the different transport regimes. The implication of the comparable values of L_s and p obtained in different regimes is twofold. There are two kinds of disorder in QAH materials, one is the quenched disorder (crystalline defects, Cr doping disorder, Bi-Sb alloying disorder, etc.) and the other is the disorder from the magnetic domain structure. When the system is in the QAH regime, the magnetism is in a single domain, whereas the system features an even population of randomly distributed up and down magnetic domains in the insulating regime⁴⁷. Thus, while the quenched disorder is fixed, disorder from magnetic domains changes from maximally ordered to maximally disordered when the system is tuned from the QAH to the insulating regime. Since L_s is unchanged during the phase transition, the results above clearly indicate that the dominant inelastic scattering occurs from quenched disorder, with no apparent contribution from the disordered magnetic domain structure in the insulating phase. Meanwhile, the observation of the constant critical exponent p indicates the nature of the interaction between electrons and these disorders is unchanged through the quantum phase transition.

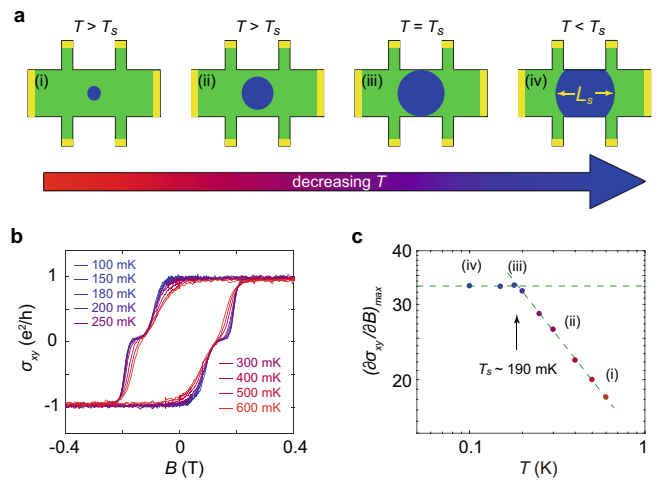


Fig. 4 Saturation of $(\partial\sigma_{xy}/\partial B)_{\max}$ in the quantum critical regime at low temperatures for a 5- μm QAH device. a Illustration of L_s at different temperatures, green regions represent the area of the Hall-bar device and blue regions indicate the length scale of L_s . From scenario (i) to (iii), L_s grows as the temperature is lowered. In scenario (iii), L_s is comparable to the physical size of the Hall-bar device. In scenario (iv), L_s is limited by the physical size. **b** Field dependence of σ_{xy} at different temperatures, all curves were measured with a 0.5 nA current. **c** Temperature dependence of $(\partial\sigma_{xy}/\partial B)_{\max}$ in the quantum critical regime. The scaling behavior saturates at ~ 190 mK, indicating L_s reaches the physical size of the sample at this temperature. (i)–(iv) correspond to the scenarios illustrated in **a**.

Direct detection of L_s in the mesoscopic scaled QAH device. While the above approximations of L_s are relatively crude in nature, they notably suggest that standard lithographic processes may be used to fabricate devices with feature sizes comparable to the characteristic length scale of the material. For samples with a large enough size, during the phase transition, the observable quantities of the system are solely determined by the ratio of L_s and the correlation length of order parameter fluctuations ξ ^{11,12}. However, in small devices measured at sufficiently low temperatures, the material’s natural inelastic scattering length may become comparable to the physical size of the sample L , artificially bounding the effective value of L_s experienced by electrons in the device. As a consequence of this bounding, a temperature T_s will exist such that the ratio L_s/ξ , and consequentially the critical transport of the sample, will remain constant for all temperatures below T_s . Here T_s represents the point for which $L_s = L$, enabling an exact, experimental determination of L_s at this temperature (Fig. 4a).

To experimentally observe such an effect, we fabricated Hall bars with a size of $5 \mu\text{m} \times 15 \mu\text{m}$ using e-beam lithography. Figure 4b presents the field dependence of σ_{xy} for the 5- μm -sample at different temperatures, and Fig. 4c shows the temperature dependence of $(\partial\sigma_{xy}/\partial B)_{\max}$ at the quantum critical regime. Instead of the diverging increase with decreasing temperature as shown for the large sample in Fig. 2b, $(\partial\sigma_{xy}/\partial B)_{\max}$ saturates abruptly at around 190 mK. This indicates L_s reaches the physical size of the sample at this temperature. That L_s equals 5 μm at 190 mK is in good agreement with the estimation obtained from the current heating results. Note that in order to avoid the saturation caused by the current heating, a current as small as 0.5 nA was used for the measurement. To further rule out such a heating effect, we use different currents to measure at 100 mK. As can be seen in Supplementary Fig. 6, the value of $(\partial\sigma_{xy}/\partial B)_{\max}$ remains constant when the current does not exceed 0.5 nA, proving the current heating effect negligible in

the experiment. As a confirmation that this effect is reflective of the intrinsic finite-size effect, the measurement has been repeated in another 5- μm -device shown in Supplementary Fig. 7. The finite-size effect is of practical importance for the application of QAH-based electronic devices. While it is broadly desirable to fabricate more compact devices, for a coherent quantum system like QAH, the finite size limits its coherence at low temperature, significantly impacting the performance of the device. As such, special care must be taken in choosing the proper size of the devices.

Discussion

To summarize, we obtained L_s in different conduction regimes of the QAH by analyzing the current heating results. A temperature exponent $p \sim 2.1$ and a value on the order of 1 μm for L_s at 200 mK were found in all regimes, revealing a universal inelastic scattering length in QAH. Furthermore, in mesoscopic devices, we observed the finite-size effect as L_s reaches the physical size of the device at low temperatures, enabling the direct detection of L_s in QAH. Our work unveils the fundamental length scale in QAH samples, which sheds light on the understanding of mesoscopic transport in QAH materials and facilitates the implementation of dissipationless electronics in QAH-based devices.

Methods

Sample growth. The molecular beam epitaxy grown samples were prepared in a Perkin-Elmer chamber with a base vacuum of 5×10^{-10} Torr. High-purity Cr(99.995%), Bi(99.999%), Sb(99.999%), and Te(99.9999%) were deposited on the epi-ready semi-insulating GaAs(111)B substrates. The growth process was monitored using in-situ Reflection high-energy electron diffraction.

Device fabrication. Grown films were patterned into Hall bars for transport measurements. The 0.5-mm-devices were fabricated using hard masks and reactive-ion etching. The 5- μm mesoscopic devices were patterned by the e-beam lithography.

Transport measurements. Transport measurements were carried out on a Physical Property Measurement System (Quantum Design) with a dilution refrigerator insert (50 mK, 9 T).

Data availability

All data for the figures and other Supplementary information that support this work are available upon reasonable request to the corresponding author.

Received: 18 April 2022; Accepted: 6 June 2022;

Published online: 22 July 2022

References

- Lee, P. A. & Ramakrishnan, T. Disordered electronic systems. *Rev. Mod. Phys.* **57**, 287 (1985).
- Abrahams, E., Anderson, P., Licciardello, D. & Ramakrishnan, T. Scaling theory of localization: Absence of quantum diffusion in two dimensions. *Phys. Rev. Lett.* **42**, 673 (1979).
- Anderson, P., Abrahams, E. & Ramakrishnan, T. Possible explanation of nonlinear conductivity in thin-film metal wires. *Phys. Rev. Lett.* **43**, 718 (1979).
- Lin, J.-J. & Bird, J. Recent experimental studies of electron dephasing in metal and semiconductor mesoscopic structures. *J. Phys. Condens. Matter* **14**, R501 (2002).
- Aronov, A. & Sharvin, Y. V. Magnetic flux effects in disordered conductors. *Rev. Mod. Phys.* **59**, 755 (1987).
- Hikami, S., Larkin, A. I. & Nagaoka, Y. Spin-orbit interaction and magnetoresistance in the two dimensional random system. *Prog. Theo. Phys.* **63**, 707–710 (1980).
- Lee, P. A. & Stone, A. D. Universal conductance fluctuations in metals. *Phys. Rev. Lett.* **55**, 1622 (1985).
- Datta, S. *Electronic transport in mesoscopic systems*. (Cambridge University Press, 1997).
- Thouless, D. Maximum metallic resistance in thin wires. *Phys. Rev. Lett.* **39**, 1167 (1977).
- Abrahams, E., Anderson, P., Lee, P. & Ramakrishnan, T. Quasiparticle lifetime in disordered two-dimensional metals. *Phys. Rev. B* **24**, 6783 (1981).
- Huckestein, B. Scaling theory of the integer quantum Hall effect. *Rev. Mod. Phys.* **67**, 357 (1995).
- Sondhi, S. L., Girvin, S., Carini, J. & Shahar, D. Continuous quantum phase transitions. *Rev. Mod. Phys.* **69**, 315 (1997).
- Koch, S., Haug, R., Klitzing, K. V. & Ploog, K. Size-dependent analysis of the metal-insulator transition in the integral quantum Hall effect. *Phys. Rev. Lett.* **67**, 883 (1991).
- Li, W. et al. Scaling in plateau-to-plateau transition: a direct connection of quantum Hall systems with the Anderson localization model. *Phys. Rev. Lett.* **102**, 216801 (2009).
- Kawamura, M. et al. Current-driven instability of the quantum anomalous Hall effect in ferromagnetic topological insulators. *Phys. Rev. Lett.* **119**, 016803 (2017).
- Yu, R. et al. Quantized anomalous Hall effect in magnetic topological insulators. *Science* **329**, 61–64 (2010).
- Chang, C.-Z. et al. Experimental observation of the quantum anomalous Hall effect in a magnetic topological insulator. *Science* **340**, 167–170 (2013).
- Kou, X. et al. Scale-invariant quantum anomalous Hall effect in magnetic topological insulators beyond the two-dimensional limit. *Phys. Rev. Lett.* **113**, 137201 (2014).
- Mogi, M. et al. Magnetic modulation doping in topological insulators toward higher-temperature quantum anomalous Hall effect. *Appl. Phys. Lett.* **107**, 182401 (2015).
- Chang, C.-Z. et al. High-precision realization of robust quantum anomalous Hall state in a hard ferromagnetic topological insulator. *Nat. Mater.* **14**, 473–477 (2015).
- Deng, Y. et al. Quantum anomalous Hall effect in intrinsic magnetic topological insulator MnBi_2Te_4 . *Science* **367**, 895–900 (2020).
- Serlin, M. et al. Intrinsic quantized anomalous Hall effect in a moiré heterostructure. *Science* **367**, 900–903 (2020).
- Li, T. et al. Quantum anomalous Hall effect from intertwined moiré bands. *Nature* **600**, 641 (2021).
- Wang, J., Lian, B. & Zhang, S.-C. Universal scaling of the quantum anomalous Hall plateau transition. *Phys. Rev. B* **89**, 085106 (2014).
- Dykhne, A. & Ruzin, I. Theory of the fractional quantum Hall effect: the two-phase model. *Phys. Rev. B* **50**, 2369 (1994).
- Checkelsky, J. et al. Trajectory of the anomalous Hall effect towards the quantized state in a ferromagnetic topological insulator. *Nat. Phys.* **10**, 731–736 (2014).
- Kou, X. et al. Metal-to-insulator switching in quantum anomalous Hall states. *Nat. Commun.* **6**, 1–8 (2015).
- Grauer, S. et al. Scaling of the quantum anomalous Hall effect as an indicator of axion electrodynamics. *Phys. Rev. Lett.* **118**, 246801 (2017).
- Huo, Y., Hetzel, R. & Bhatt, R. Universal conductance in the lowest Landau level. *Phys. Rev. Lett.* **70**, 481 (1993).
- Shahar, D., Tsui, D., Shayegan, M., Bhatt, R. & Cunningham, J. Universal conductivity at the quantum Hall liquid to insulator transition. *Phys. Rev. Lett.* **74**, 4511 (1995).
- Chang, C.-Z. et al. Observation of the quantum anomalous Hall insulator to Anderson insulator quantum phase transition and its scaling behavior. *Phys. Rev. Lett.* **117**, 126802 (2016).
- Liu, C. et al. Distinct quantum anomalous Hall ground states induced by magnetic disorders. *Phys. Rev. X* **10**, 041063 (2020).
- Wei, H., Tsui, D., Paalanen, M. & Pruisken, A. Experiments on delocalization and universality in the integral quantum Hall effect. *Phys. Rev. Lett.* **61**, 1294 (1988).
- Pruisken, A. Universal singularities in the integral quantum Hall effect. *Phys. Rev. Lett.* **61**, 1297 (1988).
- Wei, H., Engel, L. & Tsui, D. Current scaling in the integer quantum Hall effect. *Phys. Rev. B* **50**, 14609 (1994).
- Pan, W., Shahar, D., Tsui, D., Wei, H. & Razeghi, M. Quantum Hall liquid-to-insulator transition in $\text{In}_{1-x}\text{Ga}_x\text{As}/\text{InPt}$ heterostructures. *Phys. Rev. B* **55**, 15431 (1997).
- Fox, E. J. et al. Part-per-million quantization and current-induced breakdown of the quantum anomalous Hall effect. *Phys. Rev. B* **98**, 075145 (2018).
- Song, J. & Prodan, E. Characterization of the quantized Hall insulator phase in the quantum critical regime. *Europhys. Lett.* **105**, 37001 (2014).
- Koch, S., Haug, R., Klitzing, K. V. & Ploog, K. Experiments on scaling in $\text{Al}_x\text{Ga}_{1-x}\text{As}/\text{GaAs}$ heterostructures under quantum Hall conditions. *Phys. Rev. B* **43**, 6828 (1991).
- Li, W., Csáthy, G., Tsui, D., Pfeiffer, L. & West, K. Scaling and universality of integer quantum Hall plateau-to-plateau transitions. *Phys. Rev. Lett.* **94**, 206807 (2005).

41. Saeed, K. et al. Impact of disorder on frequency scaling in the integer quantum Hall effect. *Phys. Rev. B* **84**, 155324 (2011).
42. Engel, L., Shahar, D., Kurdak, C. & Tsui, D. Microwave frequency dependence of integer quantum Hall effect: Evidence for finite-frequency scaling. *Phys. Rev. Lett.* **71**, 2638 (1993).
43. Huckestein, B. & Kramer, B. One-parameter scaling in the lowest Landau band: Precise determination of the critical behavior of the localization length. *Phys. Rev. Lett.* **64**, 1437 (1990).
44. Huckestein, B. Scaling and universality in the integer quantum Hall effect. *Europhys. Lett.* **20**, 451 (1992).
45. Xue, Y. & Prodan, E. Quantum criticality at the Chern-to-normal insulator transition. *Phys. Rev. B* **87**, 115141 (2013).
46. Priest, J., Lim, S. & Sheng, D. Scaling behavior of the insulator-to-plateau transition in a topological band model. *Phys. Rev. B* **89**, 165422 (2014).
47. Wang, W. et al. Direct evidence of ferromagnetism in a quantum anomalous Hall system. *Nat. Phys.* **14**, 791–795 (2018).

Acknowledgements

This work was supported by the NSF under Grant Nos. 1936383 and 2040737, the U.S. Army Research Office MURI program under Grant Nos. W911NF-20-2-0166 and W911NF-16-1-0472. C.E. is an employee of Fibertek, Inc. and performs in support of Contract No.W15P7T19D0038, Delivery Order W911-QX-20-F-0023. The views expressed are those of the authors and do not reflect the official policy or position of the Department of Defense or the US government. The identification of any commercial product or tradename does not imply endorsement or recommendation by Fibertek Inc. E.E. and N.N. were supported by the U.S. Department of Energy (DOE), Office of Science, Office of Basic Energy Sciences under Award Number DE-SC0021117.

Author contributions

P.D., C.E., and K.L.W. conceived the project. K.L.W. supervised the project. P.D., P.Z., and L.T. performed sample growth and characterization. G.Q. and S.K.C. fabricated the device. P.D., P.Z., and G.Q. performed transport measurements with the help of E.E. and N.N. P.D. and C.E. analyzed the data. G.Y. provided theoretical support. P.D., C.E., and K.L.W. wrote the manuscript with the inputs from all authors.

Competing interests

The authors declare no competing interests.

Additional information

Supplementary information The online version contains supplementary material available at <https://doi.org/10.1038/s41467-022-31105-w>.

Correspondence and requests for materials should be addressed to Peng Deng, Christopher Eckberg or Kang L. Wang.

Peer review information *Nature Communications* thanks the anonymous reviewer(s) for their contribution to the peer review of this work.

Reprints and permission information is available at <http://www.nature.com/reprints>

Publisher's note Springer Nature remains neutral with regard to jurisdictional claims in published maps and institutional affiliations.



Open Access This article is licensed under a Creative Commons Attribution 4.0 International License, which permits use, sharing, adaptation, distribution and reproduction in any medium or format, as long as you give appropriate credit to the original author(s) and the source, provide a link to the Creative Commons license, and indicate if changes were made. The images or other third party material in this article are included in the article's Creative Commons license, unless indicated otherwise in a credit line to the material. If material is not included in the article's Creative Commons license and your intended use is not permitted by statutory regulation or exceeds the permitted use, you will need to obtain permission directly from the copyright holder. To view a copy of this license, visit <http://creativecommons.org/licenses/by/4.0/>.

© The Author(s) 2022